Flow Turbulence Combust (2007) 78: 17–33
DOI 10.1007/s10494-006-9032-8

Combined Numerical and Experimental Investigation of a 15-cm Valveless Pulsejet

T. Geng · M. A. Schoen · A. V. Kuznetsov · W. L. Roberts

Received: 4 October 2005 / Accepted: 15 June 2006 /
Published online: 4 August 2006

Abstract The pulsejet, due to its simplicity, may be an ideal micro propulsion system. In this paper, modern computational and experimental tools are used to investigate the operation of a 15-cm overall length valveless pulsejet. Gas dynamics, acoustics and chemical kinetics are studied to gain understanding of various physical phenomena affecting pulsejet operation, scalability, and efficiency. Pressure, temperature, thrust, and frequency are measured as a function of valveless inlet and exit lengths and different geometries. At this length scale, it is necessary to run the pulsejets on hydrogen fuel. Numerical simulations are performed utilizing CFX to model the 3-D compressible vicious flow in the pulsejet using the integrated Westbrook–Dryer single step combustion model. The turbulent flow and reaction rate are modeled with the k–ε model and the Eddy Dissipation Model (EDM), respectively. Simulation results provide physical insight into the pulsejet cycle; comparisons with experimental data are discussed.

Key words pulsejet · valveless pulsejet · micro-propulsion · thermoacoustics

Nomenclature

D_a	Damköhler number, ratio of flow times to chemical times
Pr_t	turbulent Prandtl number, ratio of turbulent kinematic viscosity to turbulent thermal diffusivity
P_k	shear production of turbulence
S_E	energy source
t_{flow}	fluid timescale, k/ε
t_{chem}	chemical time scale
$\nu_{KI}^{'}$	stoichiometric coefficient for reactant I in reaction K
$\nu_{KI}^{''}$	stoichiometric coefficient for product I in reaction K

T. Geng · M. A. Schoen · A. V. Kuznetsov (✉) · W. L. Roberts
Department of Mechanical and Aerospace Engineering, North Carolina State University,
Campus Box 7910, Raleigh, NC 27695-7910, USA
e-mail: avkuznet@eos.ncsu.edu

k turbulence kinetic energy per unit mass
ε turbulence dissipation rate

1. Introduction

The pulsejet is an unsteady propulsion device that generates intermittent thrust. Due to its simple design and near constant-volume combustion, the pulsejet has received considerable research attention since the beginning of the 20th century. The first practical application of the pulsejet was the German V-1 'buzz bomb' in World War II. Based on the inlet design, pulsejets can be classified as either valved or valveless. An early study [1] on pulsejets found that the reed valves flapping at high frequencies in the valved pulsejets could be easily damaged at high temperature. This generated interest in finding more reliable designs such as valveless pulsejets to improve the performance and reliability.

In 1909, a patent was issued for a valveless pulsejet, where the reed valve was replaced with an 'aerodynamic valve' [2]. As shown in Figure 1a, a simple area constriction served to let fuel and air into the combustion chamber but prevents exhaust gases from escaping from the inlet. Although Marconnet's design couldn't completely avoid the backflow at the inlet [2], the valveless pulsejet became one of the major areas in pulsejet research, and a few designs were patented.

The U-shaped Lockwood–Hiller engine [3–6] is perhaps the most successful of the valveless designs. The inlet is bent backwards to change the flow direction and keep part of the hot gas inside the tube. When the pressure in the combustion chamber is below atmospheric, the hot gases are pushed back into the combustion chamber and ignite the reactants. This design maximizes the net thrust.

In 1990, Kentfield and Fernandes [7] designed a pressure gain pulse-combustor that has a thrust augmentation device allowing cold air to be entrained by the hot gas from the pulsejet inlet, providing thrust augmentation. Because of the near constant-volume combustion, this valveless pulsejet system was designed to replace the traditional steady flow combustors in the gas turbines to increase gas turbine performance. According to his experiments, the pulse-combustor increased the maximum pressure gain from 1.6% to 4% of the compressor absolute delivery pressure.

The pulsejet is based on the Humphrey thermodynamic cycle, where isochoric heat addition (combustion) follows an isentropic compression and isobaric heat rejection follows an isentropic expansion. However, since the wave compression is weak, the thermodynamic efficiency is low, especially compared with the Brayton cycle where mechanical compression offers very high thermodynamic efficiency. This lack of thermodynamic efficiency is somewhat offset by the fundamental simplicity of the pulsejet. For typical large-scale applications, the pulsejet is not competitive, and interest in pulsejets has been relatively low for the past 40 years. However, the thermodynamic efficiency of conventional engines (such as gas turbines) decreases non-linearly with decreasing characteristic engine scale [8, 9]. Pulsejets, especially valveless pulsejets, are attractive as candidates for miniaturization due to their simple design, leading to a resurgence in interest in pulsejets.

It is expected that pulsejets may be more difficult to operate as their size decreases due to a smaller combustion chamber volume, insufficient mixing, and dissipation of the necessary pressure oscillations. The scalability is a function of the inlet length,

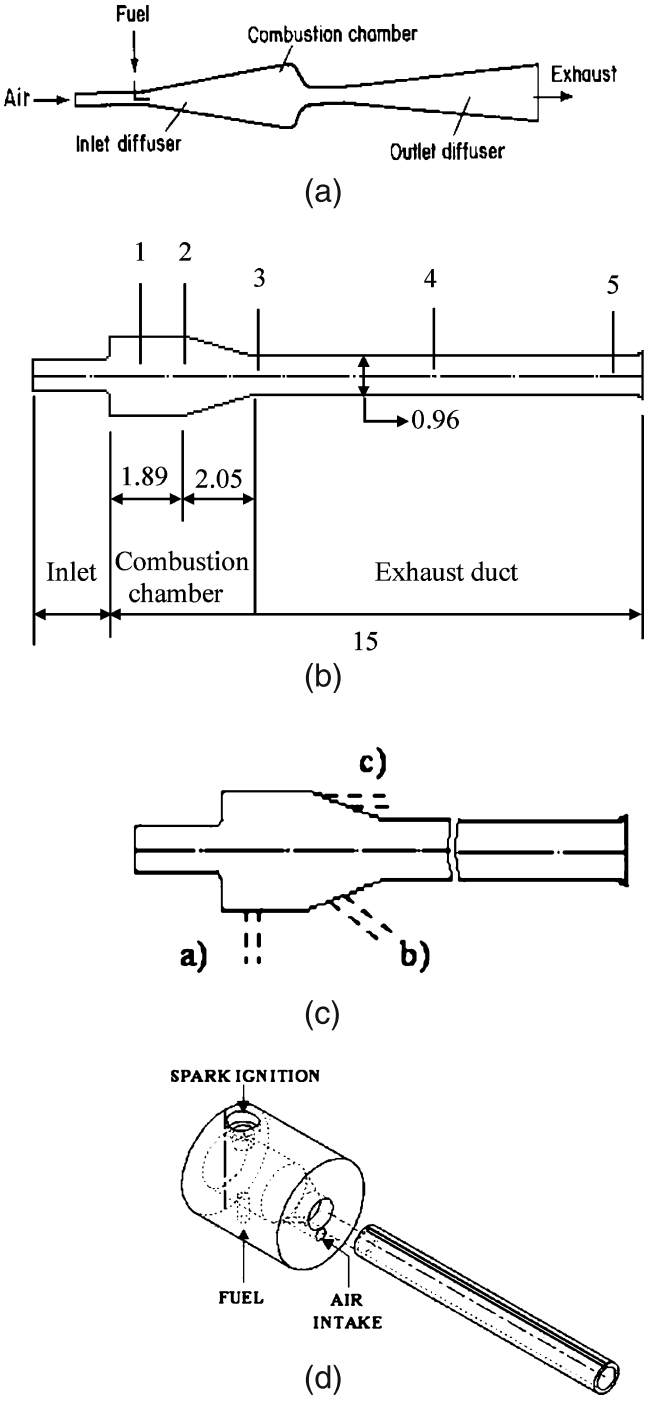

Figure 1 (**a**) Marconnet's design with the aerodynamic valve (**b**) 15 cm valveless pulsejet geometry and dimensions (cm) (**c**) The inlet orientations **a** 90° **b** 135° **c** 180° (**d**) The combustion cylinder components.

area ratio between the inlet and the combustion chamber, and the exhaust duct length. It is not practical to test all the possible geometries with different parameter values, therefore CFX is used to simulate the operation of the pulsejet and provide a detailed understanding of the interacting chemical kinetic, fluid mechanic, and acoustic processes occurring in the small scale pulsejet.

2. Experimental Apparatus and Setup

The valveless pulsejet investigated in this research is a scaled down version of the BMS (Bailey Machining Service) hobby-scale pulsejet. To the best of our knowledge, this is the first research that reports a valveless pulsejet of such a small size. As shown in Figure 1b, the valveless pulsejet consists of three sections: The inlet, the combustion chamber (a constant-area section and a transition section), and the exhaust duct. Five ports were added to allow measurement of the pressure and temperature at various axial locations (they were placed 1.0, 2.0, 4.5, 8.8, and 14.0 cm from the beginning of the combustion chamber). These locations correspond to immediately after the location of direct fuel injection, just before the transition section, just after the transition section, halfway down the exhaust tube, and just before the exit plane, respectively.

Different inlet area to exit area ratios (0.13, 0.09, and 0.04) and inlet lengths (5.08, 3.81, 2.54, and 1.27 cm) were tested. Fuel was continuously injected into the combustion chamber and air entered the combustion chamber whenever the pressure was lower than the ambient pressure, i.e., the pulsejet was naturally aspirated. A mini spark plug was used to ignite the air–fuel mixture initially. After several combustion events, fuel and air mixture was ignited by contact with the residual hot products in the pulsejet and the hot walls. Thus, the spark plug was only required to initiate the combustion during the first few cycles. All cases were running in an environment of 1 atm pressure and approximately 300 K temperature.

Both rotometers and mass flow meters were used to measure fuel flow rates. Airflow rates were not measured. Fast response pressure transducers were used to measure the instantaneous pressure. B-type thermocouples were used to measure average gas temperature inside the jet at various axial locations. Time resolved thrust was measured via a piezoelectric load cell. The load cell was exposed to shear loads in the direction of positive and negative thrust. The required preload was achieved by compressing the load cell between two aluminum plates.

3. Numerical Model

The current study models unsteady, three-dimensional, compressible, viscous flow with heat transfer, combustion, and radiation. The geometry and dimensions of the jet model used in computations exactly corresponds to that used in experiments; this enables direct comparison between experimental and numerical results and validation of computational results by our experiments. CFX5.7 software package was utilized. The second order transient scheme and high-resolution advection scheme were used to capture the compression/expansion waves. The timestep was chosen such that the Courant number was unity and the solution had a convergence criterion of 10^{-4} in residual mean square value.

The computations were performed on the NC State IBM Blade center utilizing a single 3.0 GHz Inter Xeon processor. Typical computational time for one cycle of the pulsejet was 4.3 CPU hours. The turbulent flow was simulated using a k–ε model based on the Reynolds Averaged Navier–Stokes (RANS) equations. The k–ε model was validated by comparing the experimental data with simulation data for operation frequency, pressure, and average temperature. Previous work [10] had shown that k–ε model gives the smallest error in predicting jet operation frequency; for example, the error is within ±5% for a 50 cm valved pulsejet operating at a measured frequency of 232 Hz [10]. The Westbrook–Dryer single-step reaction model with EDM was used to simulate the combustion process [11]. The viscous effect in the boundary layer region was modeled by the log-law, in which the empirical formulas were provided to connect the wall conditions to the dependent variables at the near-wall mesh node.

3.1. Model of turbulent flow and heat transfer

Governing equations for the fluid flow are given below. The continuity equation is:

$$\frac{\partial \rho}{\partial t} + \Delta \cdot (\rho U) = 0 \tag{1}$$

the momentum equation based on the eddy viscosity assumption and is given by

$$\frac{\partial \rho U}{\partial t} + \nabla \cdot (\rho U \otimes U) = \nabla p' + \nabla \cdot [\mu_{\text{eff}} (\nabla U + (\nabla U)^T)] \tag{2}$$

where μ_{eff} is the total viscosity that accounts for turbulent viscosity, and p' is the modified pressure given by

$$p' = p + \frac{2}{3}\rho k \tag{3}$$

The k–ε model is based on the eddy viscosity concept, which assumes:

$$\mu_{\text{eff}} = \mu + \mu_{\text{t}} \tag{4}$$

where μ_{t} is the turbulent viscosity:

$$\mu_{\text{t}} = \mathrm{C}_{\mu} \rho \frac{\mathrm{k}^2}{\epsilon} \tag{5}$$

The k–ε model includes the following equations for the kinetic energy, k, and the dissipation rate of turbulence, ε:

$$\frac{\partial(\rho \mathrm{k})}{\partial \mathrm{t}} + \nabla \cdot (\rho \mathrm{U k}) = \nabla \cdot \left[\left(\mu + \frac{\mu_{\text{t}}}{\sigma_{\mathrm{k}}} \right) \nabla \mathrm{k} \right] + \mathrm{P_k} - \rho \epsilon \tag{6}$$

$$\frac{\partial(\rho \epsilon)}{\partial \mathrm{t}} + \nabla \cdot (\rho \mathrm{U} \epsilon) = \nabla \cdot \left[\left(\mu + \frac{\mu_{\text{t}}}{\sigma_{\epsilon}} \right) \nabla \epsilon \right] + \frac{\epsilon}{\mathrm{k}} (\mathrm{C}_{\epsilon 1} \mathrm{P_k} - \mathrm{C}_{\epsilon 2} \rho \epsilon) \tag{7}$$

where $\mathrm{C}_{\epsilon 1}$, $\mathrm{C}_{\epsilon 2}$, σ_{k}, and σ_{ϵ} are model constants (their values are given in Table I) and $\mathrm{P_k}$ is the turbulence production due to the viscous force:

$$\mathrm{P_k} = \mu_{\text{t}} \nabla \mathrm{U} \cdot (\nabla \mathrm{U} + \nabla \mathrm{U}^{\mathrm{T}}) - \frac{2}{3} \nabla \cdot \mathrm{U} (3 \mu_{\text{t}} \nabla \cdot \mathrm{U} + \rho \mathrm{k}) \tag{8}$$

Table I Values of various model constants used in simulations.

Symbol	Description	Dimensions	Value
A	Eddy dissipation model coefficient	1	4.0
B	Eddy dissipation model coefficient	1	0.5
$C_{\epsilon 1}$	k–ε turbulence model constant	1	1.44
$C_{\epsilon 2}$	k–ε turbulence model constant	1	1.92
σ_k	Turbulent model constant for the k equation	1	1.0
σ_ϵ	k–ε turbulence model constant	1	1.3
C_μ	k–ε turbulence model constant	1	0.09

The energy equation is:

$$\frac{\partial \rho(h + \frac{1}{2}U^2 + k)}{\partial t} - \frac{\partial P}{\partial t} + \nabla \cdot \left[\rho \mathbf{U}\left(h + \frac{1}{2}U^2 + k\right)\right] = \nabla \cdot \left(\lambda \nabla T + \frac{\mu_t}{Pr_t}\nabla h\right) + S_E \tag{9}$$

3.2. Eddy dissipation model for combustion

The EDM, which was utilized to model the combustion, assumes that either reaction is fast compared to turbulent mixing (high Damköhler number is assumed), or reaction rate is proportional to the time scale of turbulent mixing. The time scale of turbulent mixing, which depends on the eddy properties, is determined as the ratio of k and ε.

The reaction rate was determined from the minimum of expressions (10) and (11) below:

$$R_k = A\frac{\epsilon}{k}\min\left(\frac{[I]}{v'_{KI}}\right) \tag{10}$$

$$R_k = AB\frac{\epsilon}{k}\left(\frac{\sum_P [I]W_I}{\sum_P W_I v'_{KI}}\right) \tag{11}$$

where [I] is the molar concentration of the reactant I and P loops over all product components. A and B are model constants and their values are given in Table I. Flame extinction was also modeled by controlling the chemical time scale and extinction temperature values. The local reaction rate was set to zero if the turbulent time scale was smaller than the chemical time scale specified. In this case the chemical time scale was 0.0004 s. The turbulence time scale is calculated from the flow field as k/ϵ. The other method to determine the flame extinction is such that the flame is locally quenched whenever the temperature is less than the specified extinction temperature. Both the chemical time scale and the extinction temperature were specified to model the flame extinction.

4. Results and Discussions

4.1. The valveless pulsejet operation cycle

To illustrate 15 cm valveless pulsejet operation cycle, Figure 2 displays simulation results for the jet of the total length of 20.5 cm and the inlet area to the combustion cross-section area ratio of 0.13 (see case 1.3 in Table II). These simulation results are validated by comparison with experimental data, as shown in Section 4.3. The pulsejet is static and the wall temperature is 300 K. The pressure outside the pulsejet is atmospheric. Gas-phase hydrogen is injected into the combustion chamber with the same mass flow rate as in experiments. The operation cycle is separated into 10 steps from (1) to (10) from top to bottom shown in Figure 2. The positive direction

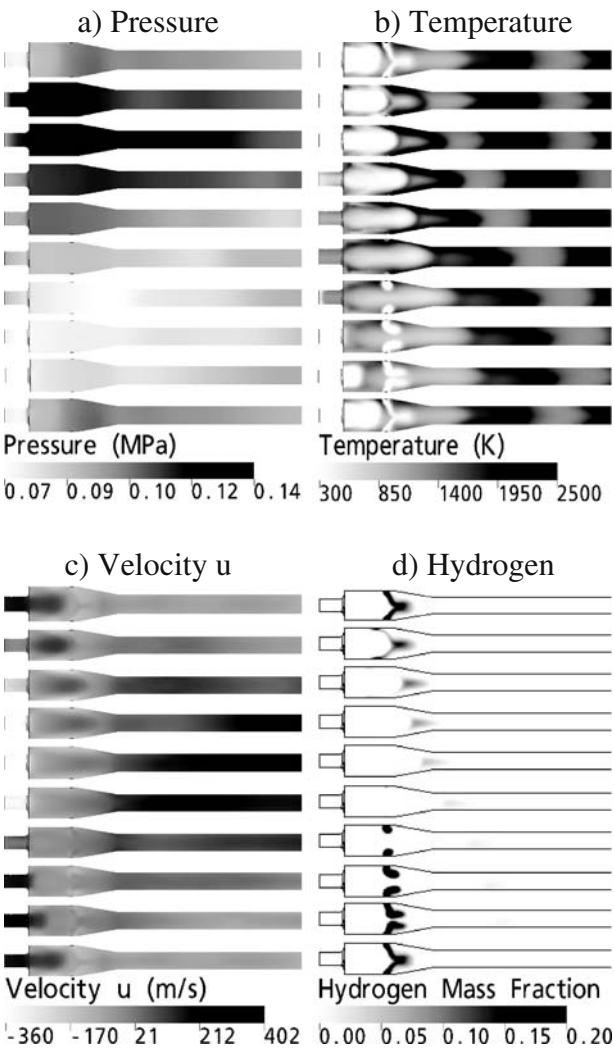

Figure 2 Simulation results for pressure and temperature: (**a**) Pressure (**b**) Temperature (**c**) Velocity u (**d**) Hydrogen mass fraction.

Table II Experimental results for the scalability study.

Case	AR	Inlet length	Exhaust duct lengths at which self-sustained combustion was achieved
	(A_i/A_c)	L_i (cm)	L (cm)
1.1	0.13	5.08	N/A
1.2	0.13	3.81	45.7, 29.2
1.3	0.13	2.54	44.5, 39.1, 33.7, 28.3
1.4	0.13	1.27	42.9, 37.5, 32.1, 26.7, 21.3, 15.9
2.1	0.09	5.08	41.2, 36.2
2.2	0.09	3.81	45.7, 34.9, 23.8
2.3	0.09	2.54	44.1, 33.0, 22.5
2.4	0.09	1.27	42.9, 31.8, 21.3, 15.6
3.1	0.04	5.08	47.0, 36.2
3.2	0.04	3.81	45.7, 34.6, 29.5
3.3	0.04	2.54	44.3, 33.3, 22.5
3.4	0.04	1.27	42.9, 32.1, 21.3, 15.9

of velocity u is defied as flow going out of the exit. For a better view of hydrogen distribution, the maximum value in the legend is set to 0.2.

(1) Combustion event occurs at the stoichiometric contour between air and hydrogen. The pressure and temperature begin to increase in the combustion chamber. The negative velocity of the cold backflow air decreases. Air continues entering the combustion chamber through the inlet, but with reduced velocity.
(2) Combustion continues causing the pressure and temperature to increase in the combustion chamber. Compression waves are generated and propagate to the inlet and the exit. When the pressure of the cold air becomes equal to the pressure of the hot gases, the velocity goes to zero at the interface of these two gases.
(3) Expansion waves are generated at the inlet and decrease pressure in the combustion chamber. A positive, increasing velocity characterizes the flow at the exit; while at the inlet, the hot products flow out with an increasing negative velocity.
(4) Expansion waves are generated at the exit and travel back to the combustion chamber. Pressure decreases in the combustion chamber and the velocity of the gases out of the inlet and the exit reach their maximum. Most of the hydrogen is oxidized by the time.
(5) The pressure in the combustion chamber keeps decreasing. Temperature increases in the inlet.
(6) The expansion waves from the exit enter the combustion chamber and further decrease the pressure in the combustion chamber. The outgoing velocity at the inlet starts to decrease.
(7) The expansion wave enters the combustion chamber and decreases the pressure below the atmospheric. Air enters the combustion chamber through the injection. Hot products continue to be expelled at the outlet but with a lower velocity.

(8) The pressure and temperature in the combustion chamber continue decreasing while the inlet velocity continues increasing. The product velocity at the exit goes to zero and actually reverses, causing backflow at the exit, resulting in a temperature decrease due to entrainment of ambient air at 300 K.
(9) Cold air from the inlet enters the combustion chamber. Hot gas in the exhaust duct is pushed back to the combustion chamber. The pressure in the combustion chamber increases.
(10) Backflow continues, but its negative velocity becomes smaller. When the pressure in the combustion chamber approaches atmospheric pressure and air from the inlet mixes with hydrogen in the combustion chamber, the next cycle begins.

In each cycle, the combustion chamber pressure is decreased by the expansion waves from both the outlet and the inlet. Compared with the valved designs [10, 12], this does not provide lower sub-atmosphere pressure in the combustion chamber due to the mass addition of the air from the inlet. The exhaust duct may contain hot gases generated by several combustion events. The cold air entering the combustion chamber creates a strong vortex that greatly accelerates the mixing process. The oxygen that reacts with hydrogen enters the combustion chamber from the inlet only, no fresh air enters the combustion chamber through the exhaust duct. From these numerical results, it is evident that the inlet design is critical to the valveless pulsejet operation, justifying the need to investigate the geometric influence of the inlet on small scale pulsejets.

4.2. Experimental scalability study

In this paper, scalability is studied by varying the inlet length, inlet inner diameter, and exhaust duct length to find the range of pulsejet lengths in which the pulsejet can be operated. Different exit geometries were also examined. For each case, the inlet to combustion chamber area ratio was held constant while varying inlet and exhaust duct lengths. For each inlet length, pulsejet operation was attempted at several exhaust lengths using identical incremental steps for each case. The results are shown in Table II. A_i and A_c in Table II denote the areas of the inlet and combustion chamber cross-sections, respectively. Table II shows that, within the tested dimension range, decreasing the inlet length increases the pulsejet scalability regardless of the area ratio.

4.2.1. *Length investigation*

Table III tabulates the shortest pulsejet lengths, per inlet configuration, that were able to achieve self-sustaining combustion. It is evident that, for a given intake area, the minimum feasible length decreases with decreasing inlet length. In other words, the jet with a shorter inlet has a wider operation range. However, for a given inlet length changing the inlet area does not have much effect on jet scalability. Table III shows that the minimum operation length is a stronger function of inlet length rather than inlet area ratio; suggesting that area ratios may only be utilized to slightly reduce inherent inlet to exhaust duct length ratios.

Minimal jet lengths are plotted in Figure 3a against inlet length to exit length ratios in order to investigate trends in behavior. The inlet length is denoted as L_i, the exhaust duct length is denoted as L_e, and the minimum overall jet length is denoted as L_{min}, AR is the area ratio of the inlet to that of the combustion chamber. For a fixed inlet length ratio the minimum feasible pulsejet length does not change much regardless of the AR. A linear increase of the minimum inlet length is observed with increasing L_i/L_e. This indicates that for a certain combustion chamber diameter, there is a critical inlet length ratio for which the pulsejet will remain self-sustaining. Inlet length ratios have actually been shown to have a significant effect on maximum hydrogen flow rates at various inlet configurations, as shown in Table IV.

4.2.2. *Pulsejet frequency*

With forced air, the pulsejet can operate over a fairly wide range of conditions. However, independent operation is much more restrictive and a function of many parameters. Figure 3b displays the effect of changing the overall jet length on the frequency, for a fixed AR value of 0.04. Similar to valved pulsejets [10, 12], the frequency of valveless pulsejets decreases with increasing the total length. Furthermore, increasing the inlet length also decreases the frequency. This is because the increased inlet length increases the minimum feasible jet length, as shown above. Thus, the total jet length also increases, which decreases the frequency. This phenomenon is also observed in experiments with different AR values.

Figure 4 shows how AR affects frequency with a fixed inlet length. It is evident that increasing the inlet area leads to increasing the frequency of the valveless pulsejet. The pulsejet with larger inlet area operates for larger length ranges.

4.2.3. *Fuel flow investigation*

As shown in Table IV, where configuration A denotes a constant exhaust length at 38 cm and configuration B denotes the minimum exhaust duct length to achieve successful operation, the larger the AR, the higher the maximum fuel flow rate, and hence throttleability. At the smallest AR of 0.04, the maximum fuel flow rate is the lowest and is relatively insensitive to either inlet length or exhaust duct length. For other ARs, the fixed exhaust duct length (A) typically has a lower $\dot{m}_{f,max}$ than for case B. The highest $\dot{m}_{f,max}$ tend to occur with the two intermediate length inlets.

Case B, which has the minimum exhaust duct length, has a larger throttleability range. This can be explained by the accompanying increase in operating frequency associated with a decrease in total length. If higher frequencies permit more com-

Table III Minimum feasible pulsejet lengths for corresponding inlet configurations.

		AR		
		0.13	0.09	0.04
Inlet length, L_i (cm)	1.27	15.86	15.56	15.86
	2.54	22.54	18.10	18.42
	3.81	24.77	19.69	25.40
	5.08	31.15	31.43	32.07

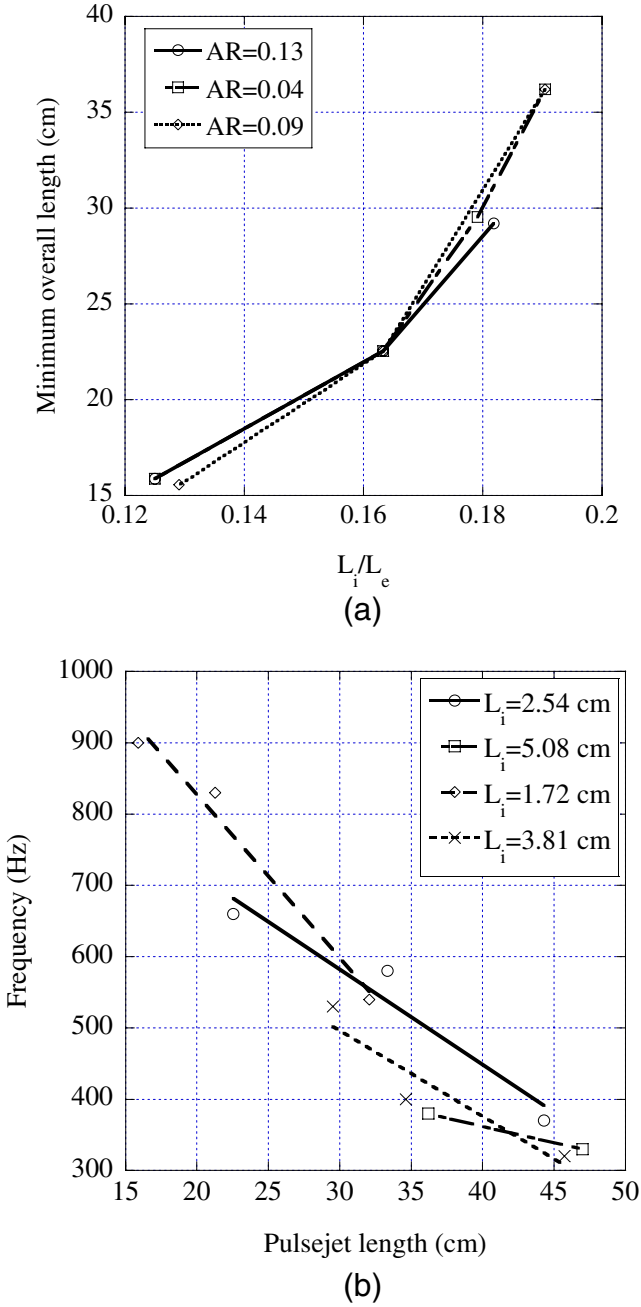

Figure 3 (**a**) Minimum feasible pulsejet lengths *versus* inlet to exit length ratios. (**b**) Frequency *versus* pulsejet length for a 0.04 inlet area ratio.

bustion events per minute, then a higher fuel consumption rate may be related to a decrease in total jet length.

Table IV Maximum H2 flow rates at various inlet configurations.

		AR					
		0.13		0.09		0.04	
		A	B	A	B	A	B
Inlet length, L_i (cm)	1.72	0.067	0.067	0.038	0.049	0.012	0.013
	2.54	0.035	0.083	0.023	0.057	0.012	0.023
	3.81	0.034	0.076	0.030	0.052	0.012	0.012
	5.08	0.033	0.060	0.026	0.034	0.012	0.013

A for a constant exhaust duct length of 38.1 cm, *B* for minimum feasible pulsejet lengths. All measurements are in gram per second.

4.3. Comparison between the simulations and the experiments

To validate the CFX code, two simulations were conducted and the results were compared with experimental data. Figure 5a shows the experimental result of the case 1.3 in Table II with a 22.5 cm total length. Chamber pressure (port 2) generally remained in the ±0.02 MPa range, while thrust is in the ±2.0 N range. The frequency is 1,010 Hz and the mean temperature in the combustion chamber is 1,550 K. Figure 5b is the result of case 1.3 with a 34.3 cm total length. The chamber pressure generally remained in the ±0.02 MPa range, while thrust decreased to ±1.2 N. The operation frequency is 830 Hz and the mean temperature in the combustion chamber is 1,520 K.

The corresponding simulation results are shown in Figure 6. The simulation domain contains approximately 40,000 elements. The turbulence was modeled using

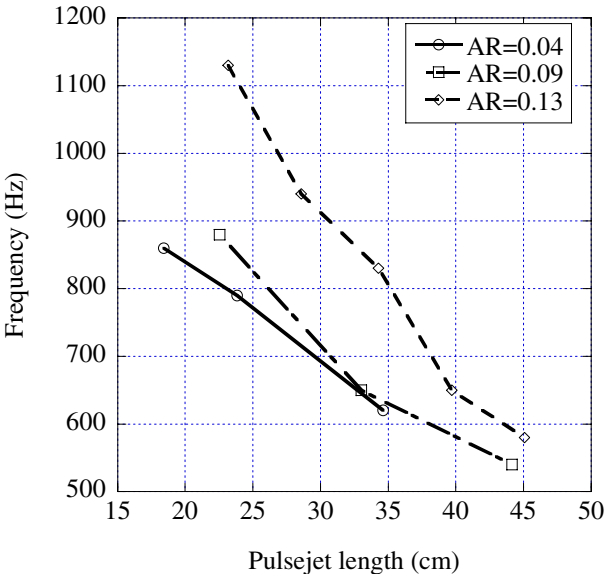

Figure 4 Fifteen-centimeter pulsejet operation frequency *versus* total length for different inlet area ratios, $L_i = 2.54$ cm.

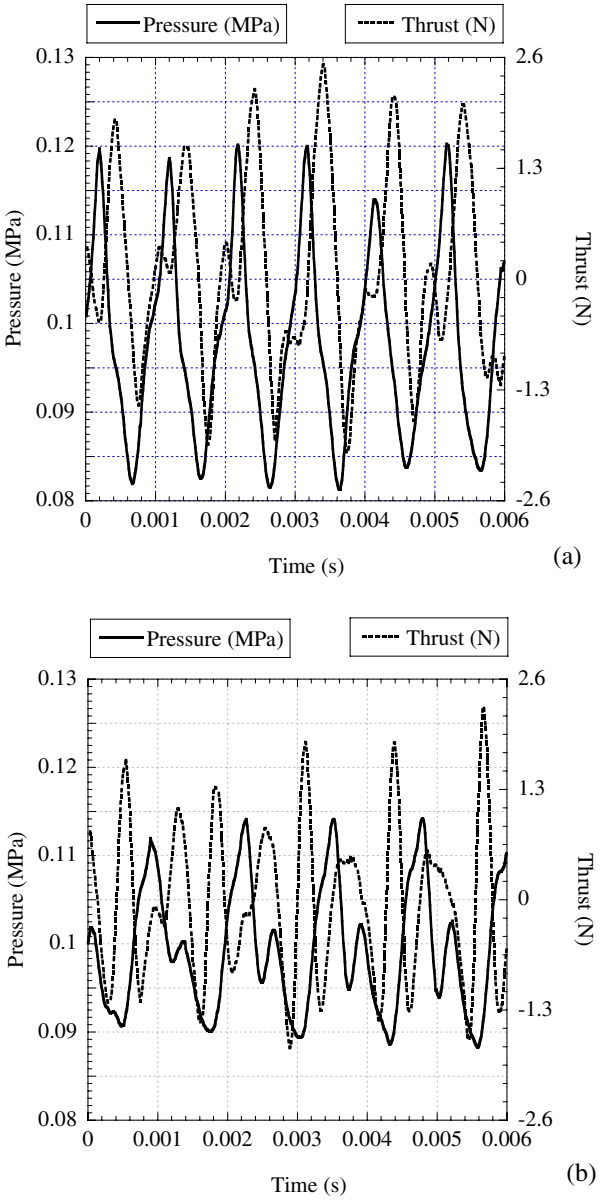

Figure 5 Experimentally measured pressure at port 2 and thrust for an area ratio of 0.13 and 2.54-cm inlet (**a**) 22.5 cm total length (**b**) 34.3 cm total length.

the k–ε model and the Eddy Dissipation Model was used for the combustion. Static thrust was calculated by summing the thrusts generated at both the inlet and the outlet [13]. At each end, only momentum thrust was calculated since the pressure difference to the ambient pressure is negligible. The average mass flow rate of hydrogen was 0.016 g/s, which was the same as in experiments.

The simulated pressure is in the ±0.02 MPa range correspondent to the experimental results and thrust is in the ±0.8 N for the 22.5-cm jet and ±1 N for the 34.3-cm

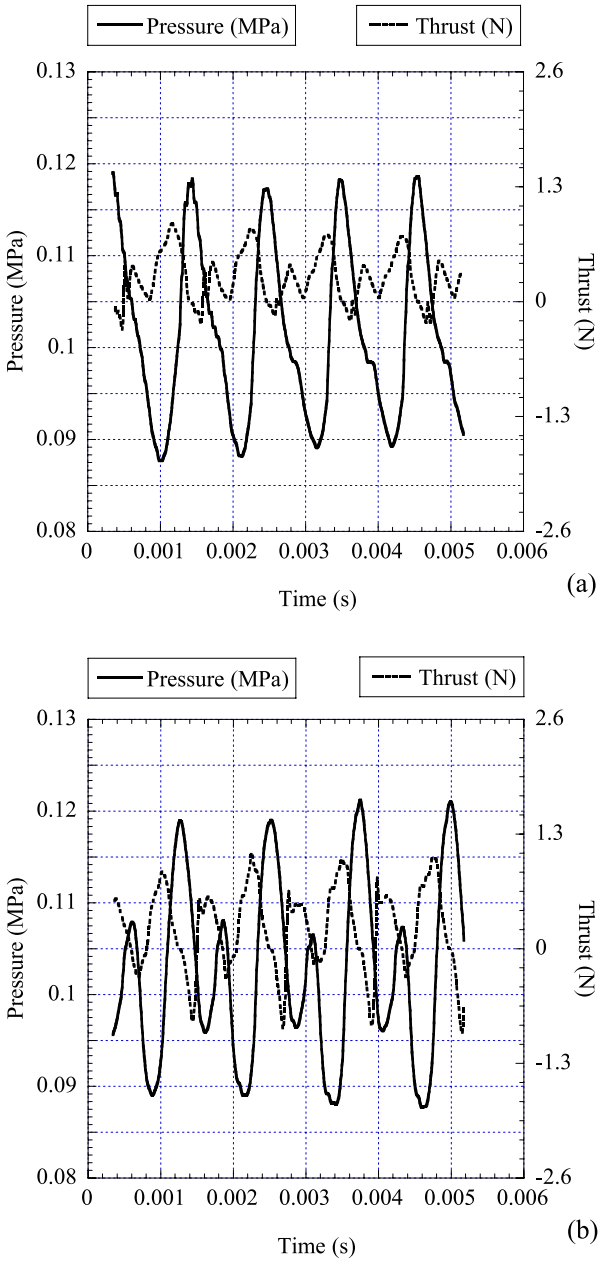

Figure 6 Simulation results of pressure at port 2 and thrust for an area ratio of 0.13 and 2.54 cm inlet (**a**) 22.5 cm total length (**b**) 34.3 cm total length.

jet. The operation frequency for Figure 6a is 1,080 and 806 Hz for Figure 6b. The assumption that pressure at both the inlet and the exhaust duct ends is exactly atmospheric may cause some inaccuracy in predicting thrust. The error in predicting frequency is 7% for the 22.5 cm jet and 3% for the 34.3 cm jet. Also notable is the ability of the model to capture the complex structure of the pressure oscillations.

In Figures 5a and 6a, it is clear that the pressure is not exactly sinusoidal. There is a component at the same frequency but slightly offset in time as the decreasing pressure side of the oscillation. In Figures 5b and 6b, the offset is nearly 180° and this secondary oscillation is very clear.

4.4. Inlet orientation

Three different valveless inlet orientations were also investigated to maximize net thrust [14]. Pulsejet operation was achieved with a 90° orientated inlet (Figure 2c, configuration a) at a 0.04 inlet area ratio. For an inlet length of 2 cm, pulsejet operation was achieved at a minimum jet length of 25.2 cm. Fuel flow rate was limited within the range of 0.017 to 0.023 g/s. A maximum overall length of 33.7 cm was found successful for the 90-degree configuration. At the longer length, the throttle ability limits increased to between 0.014 and 0.025 g/s.

In addition, tests were performed with an inlet orientated 135° (Figure 2c, configuration b), perpendicular with the slope of the transition section. An inlet area ratio of 0.04 was tested at jet lengths of 50.0, 33.6, 25.2, and 22.5 cm. The inlet was approximately 0.7 cm long. All lengths allowed pulsejet operation except for the shortest length of 22.5 cm. At 25.2 cm, the pulsejet was difficult to start and was only operable for a number of seconds at a fuel flow rate of about 0.014 g/s before cutting out.

To study reverse inlet operation, whereabouts thrust is conserved by directing inlet and exit momentum in the same direction, a new jet design was developed. As Figure 1d illustrates, a single steel 'combustion cylinder' component replaced both the combustion chamber and transition sections of the conventional scaled down BMS jet.

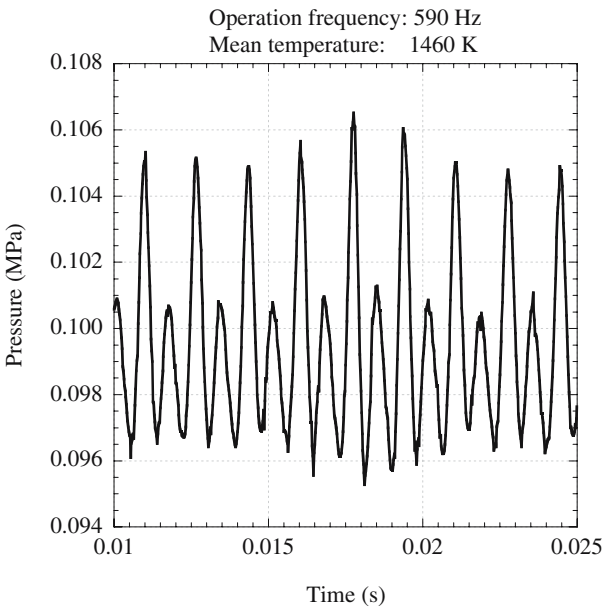

Figure 7 Pulsejet combustion chamber pressure for an opposed-facing inlet configuration with a 0.04 collective area ratio.

Three holes were drilled in the opposing face of the combustion cylinder to create inlets that faced 180° (Figure 2c, configuration c) from the conventional valveless inlet position. The inlet lengths were approximately 0.89 cm long each and the collective inlet area ratio was 0.04. Pressure and temperature were simultaneously recorded for a jet length of 37.5 cm and the results are plotted in Figure 7. Compared with the pressure profiles measured in the conventional valveless pulsejets, there is a secondary pressure rise in each cycle of the reverse-facing inlets. This is probably caused by the compression wave being reflected from the left wall of the combustion chamber.

5. Conclusions

In order to ascertain the scalability characteristics of the valveless pulsejet engine, it is necessary to first investigate the viability of operation under a range of configurations for an individual class of engine sizes. Investigation of the 15 cm class valveless pulsejet is a vital stepping stone to bridge the gap between micro-scaled pulsejet engines and the hobby-scaled engines. This research classifies the physical effects of pulsejet geometries on engine performance. To determine characteristics of performance, the chamber pressure and temperature, thrust, and operation frequency were measured. Numerical simulations are used to provide a detailed understanding of the flow behavior in the valveless pulsejet cycle. The simulation results are validated by the experimental results. This study is unique in that it represents the first detailed investigation of a valveless pulsejet engine in this size class, the smallest size known running up to date. The relevant conclusions drawn from this work are as follows:

1. The numerical model, validated by the experimental results, shows:
    a. The expansion waves from the outlet are able to enter the combustion chamber before the next cycle.
    b. In each cycle, the combustion chamber pressure is decreased by the expansion waves from the outlet and the inlet as well. The backflow from the exhaust duct cannot travel to the combustion chamber, and the oxygen for the reaction is provided by the airflow from the inlet only.
    c. The exhaust duct may contain hot gases generated by several successive combustion events. This behavior is not observed in the valved pulsejet. The cold air entering the combustion chamber creates a strong vortex that greatly accelerates the mixing process.
2. Exhaust duct length and inlet length are directly coupled in the valveless pulsejet.
    a. Pulsejet operation at minimum overall lengths was achieved with the shortest inlet lengths.
    b. Pulsejet operation at longer jet lengths was achieved with longer inlet lengths and smaller inlet area ratios.
    c. Maximum exhaust duct lengths exist for corresponding inlet lengths and area ratios. Results suggest that for given a valveless configuration, there exists a critical length above which pulsejet operation cannot be achieved.
3. Minimum exhaust duct length can be further reduced (from a constant area geometry) by about 16% on average with the addition of a diverging exit nozzle.

4. Pulsejet operation was achieved from 90°, 135°, and 180° inlet orientations with respect to the conventional forward facing valveless design.
5. Preliminary tests indicate that valveless pulsejets with multiple opposed facing inlets present similar behavioral characteristics as those of conventional design. It also may be concluded that the consolidated inlet area ratio of multiple inlets is comparable to that of a single rearward-facing inlet, taking into consideration inlet placement and internal direction of inlet flow.
6. The two main parameters determining the success of a pulsejet to operate are chemical kinetic time *versus* jet length and inlet area to combustor area ratio. At shorter lengths, the chemical kinetic reaction rate (combustion time) becomes challenged by the period of fluid mechanic oscillations. This would explain why fuels with longer chemical time scales such as propane did not permit pulsejet operation in smaller jet sizes.

Acknowledgments This project is sponsored by the Defense Advanced Research Projects Agency (DARPA) under the supervision of Dr R L. Rosenfeld, Grant No. HR0011-0-1-0036. The content of the information does not necessarily reflect the position or policy of the Government and no official endorsement should be inferred. The authors would also like to thank Dr Terry Scharton and Dr Vincent Castelli for their helpful comments and suggestions.

References

1. Tsien, H. (ed.): Jet Propulsion, Guggenheim Aero. Lab. (1946)
2. Ogorelec, B.: Valveless Pulsejet Engines. URL: http://www.pulse-jets.com/valveless/
3. Lockwood, R.M.: Advanced Research Division Report No. 508. Hiller Aircraft Co. (1963)
4. Lockwood, R.M., Patterson, W.G.: Advanced Research Division Report No. ARD-307, U. S. Army TRECOM Report 64-20. Hiller Aircraft Co., (1964)
5. Logan, J.G.: Project SQUID Tech. Memo. No. CAL-42. Cornell Aeronaut. Lab., (1951)
6. Logan, J.G.: Project SQUID Tech. Memo. No. CAL-27. Cornell Aeronaut. Lab., (1949)
7. Kentfield, J.A.C., Fernandes, L.C.V.: Improvements to the performance of a prototype pulse, pressure-gain, gas turbine combustor. J. Eng. Gas Turbines Power **112**, 67–72 (1990)
8. Waitz, I.A., Gauba, G., Tzeng, Y.: Combustors for micro-gas turbine engines. J. Fluids Eng. **120**, 109–117 (1998)
9. Spadaccini, C.M., Mehra, A., Lee, J., Zhang, X., Lukachko, S., Waitz, I.A.: High power density silicon combustion systems for micro gas turbine engines. J. Eng. Gas Turbines Power **125**, 709–719 (2003)
10. Geng, T., Kiker, A., Ordon, R., Schoen, M., Kuznetsov, A.V., Scharton, T. Roberts, W.L.: Experimentation and Modeling of Pulsed Combustion Engines. 4th Joint Meeting of the US Sections of the Combustion Institute, Philadelphia, (2005)
11. Westbrook, C.K., Dryer, F.L.: Simplified reaction mechanisms for the oxidation of hydrocarbon. Combust. Sci. Technol. **27**, 31–43 (1981)
12. Wan, Q., Roberts, W.L., Kuznetsov, A.V.: Computational analysis of the feasibility of a micro-pulsejet. Int. Commun. Heat Mass Transfer **32**, 19–26 (2005)
13. Shepherd, D.G.: Aerospace Propulsion. American Elsevier, New York (1972)
14. Schoen, M.: Experimental Investigations in 15 Centimeter Class Pulsejet Engines. Master dissertation, Mechanical and Aerospace Engineering Department, North Carolina State University, Raleigh, North Carolina, (2005)